


Cite this: *Nanoscale Adv.*, 2020, 2, 2192

# A nano-integrated diagnostic and therapeutic platform with oxidation–reduction reactions in tumor microenvironments†

Lei Zhao,<sup>ab</sup> Guihua Qiu,<sup>a</sup> Kai Wang,<sup>a</sup> Hu Chen,<sup>a</sup> Fengkai Ruan,<sup>a</sup> Nan Liu,<sup>a</sup> Zifeng Deng,<sup>a</sup> Youliang Yao,<sup>a</sup> Dongbei Guo,<sup>a</sup> Dai Wang,<sup>a</sup> Li Sha,<sup>b</sup> Xiangyu Kong,<sup>b</sup> Wenzhi Liu<sup>\*b</sup> and Yongxing Zhang <sup>\*a</sup>

In the present study, we developed a nano-integrated diagnostic and therapeutic platform with oxidation–reduction reactions in tumor microenvironments (TMEs). The proposed platform resolved the contradiction of particle size between the enhanced permeability and retention (EPR) effect and tumor interstitial penetration, as well as poor circulation and low drug-loading efficiency. Flower-like MnO<sub>2</sub> NPs were used as the core and modified with hyaluronate (HA) and H<sub>2</sub>PtCl<sub>6</sub> to obtain MnO<sub>2</sub>–HA@H<sub>2</sub>PtCl<sub>6</sub> (MHP). The maximum drug-loading efficiency rate of H<sub>2</sub>PtCl<sub>6</sub> reached 35% due to its chelation with HA. MHP showed satisfactory integrity and stability during circulation and can also be used as a magnetic resonance imaging (MRI) contrast agent. In addition, MHP as a radiosensitizer achieved an excellent tumor inhibition effect in combination with radiotherapy. Importantly, MHP released ultra-small nanoparticles, USNPs, (~20 nm) through the supramolecular self-assembly abilities of Mn<sup>2+</sup>, HA, and H<sub>2</sub>PtCl<sub>6</sub> in TMEs, leading to the increase of penetration into multicellular spheres and solid tumors (Scheme), as well as prolonging its retention in tumors.

Received 16th December 2019  
Accepted 7th March 2020

DOI: 10.1039/c9na00786e

rsc.li/nanoscale-advances

## 1 Introduction

The transportation of nanoparticles (NPs) in solid tumors is mainly associated with their diameter and surface potential.<sup>1–4</sup> A dense extracellular matrix, high interstitial fluid pressure (IFP), and uneven distribution of tumor vessel diameter are the main reasons for poor clinical treatment.<sup>5,6</sup> NPs with diameters in the range of 60–100 nm have shown a satisfactory enhanced permeability and retention (EPR) effect and high tendency towards extravasation across the tumor vessels, while they cannot uniformly and effectively penetrate into the tumor stroma.<sup>3,7</sup> The NPs with diameters in the range of 10–20 nm can significantly penetrate into the tumor stroma and spread evenly, while the removal rate is faster, and the retention time of tumor is shortened.<sup>5</sup>

Radiation therapy is a therapeutic method, utilizing ionizing radiation to induce DNA damage to kill cancer cells.<sup>8</sup> Besides, its disadvantages mainly include lack of selectivity of radiation location and poor efficacy due to the hypoxic regions in solid tumors.<sup>9</sup>

In order to solve the above mentioned problems, radiosensitizers (*e.g.*, gold nanoparticles<sup>10</sup> and titanium oxide nanoparticles<sup>11</sup>) have been developed. However, a number of these nanoparticles are not biodegradable and cannot be therefore used in clinical practice due to their long-term retention *in vivo*. It has been reported that the nanomaterial perfluorocarbon is helpful to transport oxygen, but there are a number of shortcomings, such as short retention time of oxygen in nanomaterials, low efficiency of oxygen transport, and the need for a particular range of temperature to control and release.<sup>12</sup> It is well-known that high concentration reactive oxygen species (ROS) (*e.g.*, H<sub>2</sub>O<sub>2</sub>, ~100 μM) in tumor microenvironments (TMEs) can limit the efficacy of radio-chemotherapy in tumors.<sup>13</sup> Moreover, M2 phenotype tumor-associated macrophages (TAMs) promote tumor metastasis and drug resistance in hypoxic regions and tumor hypoxic environments.<sup>14</sup>

In the present study, we synthesized a biodegradable nano-integrated diagnosis and treatment platform, namely MHP, in order to overcome the above-mentioned problems. For this purpose, hyaluronan (HA), as a hydrophilic polysaccharide, was used to modify the surface of flower-like MnO<sub>2</sub> cores and increase the loading rate of H<sub>2</sub>PtCl<sub>6</sub>. MHP is sensitive to oxidation–reduction reactions and has acceptable biocompatibility and can be utilized as an ultra-small nanoparticle (USNP) triggered by TMEs. With consuming excessive endogenous H<sub>2</sub>O<sub>2</sub> in TMEs, it degrades from the original parental NPs (100 nm) to USNPs (~20 nm), leading to deeper penetration and longer retention in the tumor stroma. Due to its initial

<sup>a</sup>State Key Laboratory of Molecular Vaccinology and Molecular Diagnostics, School of Public Health, Xiamen University, Xiamen, Fujian, 361102, PR China. E-mail: z63y94x@xmu.edu.cn

<sup>b</sup>Affiliated Zhongshan Hospital of Dalian University, Dalian, Liaoning, 116001, PR China. E-mail: liuwenzhi196507@163.com

† Electronic supplementary information (ESI) available. See DOI: 10.1039/c9na00786e



appropriate hydrodynamic diameter (100 nm), MHP has a promising EPR effect. MHP as a radiosensitizer can achieve an effective tumor inhibition in combination with radiotherapy. In addition, by means of multi-elemental and spectral detection, we preliminarily confirmed the basic components of the USNPs by combining different centrifugation and dialysis methods. Our research was conducted on the basis of the formation of USNPs by supermolecular recombination after the metabolism of nanomaterials induced by TMEs, aiming to provide a new idea for penetration of radio-chemotherapy into clinical tumors.

## 2 Results and discussion

### 2.1 Synthesis and characterization

In the current research, we synthesized  $\text{MnO}_2\text{-HA@H}_2\text{PtCl}_6$  nanoparticles by the layer-by-layer (LBL) method as a nanoscale coating and surface functionalization technique. Next, oleic

acid was utilized to reduce potassium permanganate to obtain flower-like  $\text{MnO}_2$  NPs with a size of 70–110 nm (average size: 90 nm) (Fig. 2b), and then, they were characterized by transmission electron microscopy (TEM; Fig. 1a) and (EDS; Fig. S1†).

Afterwards, the HA was adsorbed on the surface of  $\text{MnO}_2$  to form  $\text{MnO}_2\text{-HA}$ . A number of scholars demonstrated that HA possesses a series of appropriate properties, such as biocompatibility, biodegradability, and non-immunogenicity.<sup>15,16</sup> TEM revealed that core- $\text{MnO}_2$  was surrounded by light-colored substances (Fig. 1b), suggesting that HA has been successfully loaded around the core. Zeta potential almost showed the same surface charge as HA (Fig. 1i), suggesting that the combination of HA and core- $\text{MnO}_2$  is electrostatic adsorption.

Before final loading, we tested the inhibitory effect of  $\text{H}_2\text{PtCl}_6$  on cancer cells. It was disclosed that treatment with  $10 \mu\text{g mL}^{-1}$   $\text{H}_2\text{PtCl}_6$  could significantly inhibit the proliferation of HCT-116, and treatment with  $20 \mu\text{g mL}^{-1}$   $\text{H}_2\text{PtCl}_6$  for 48 h could inhibit cell proliferation by within 45% (Fig. 1e). Additionally,

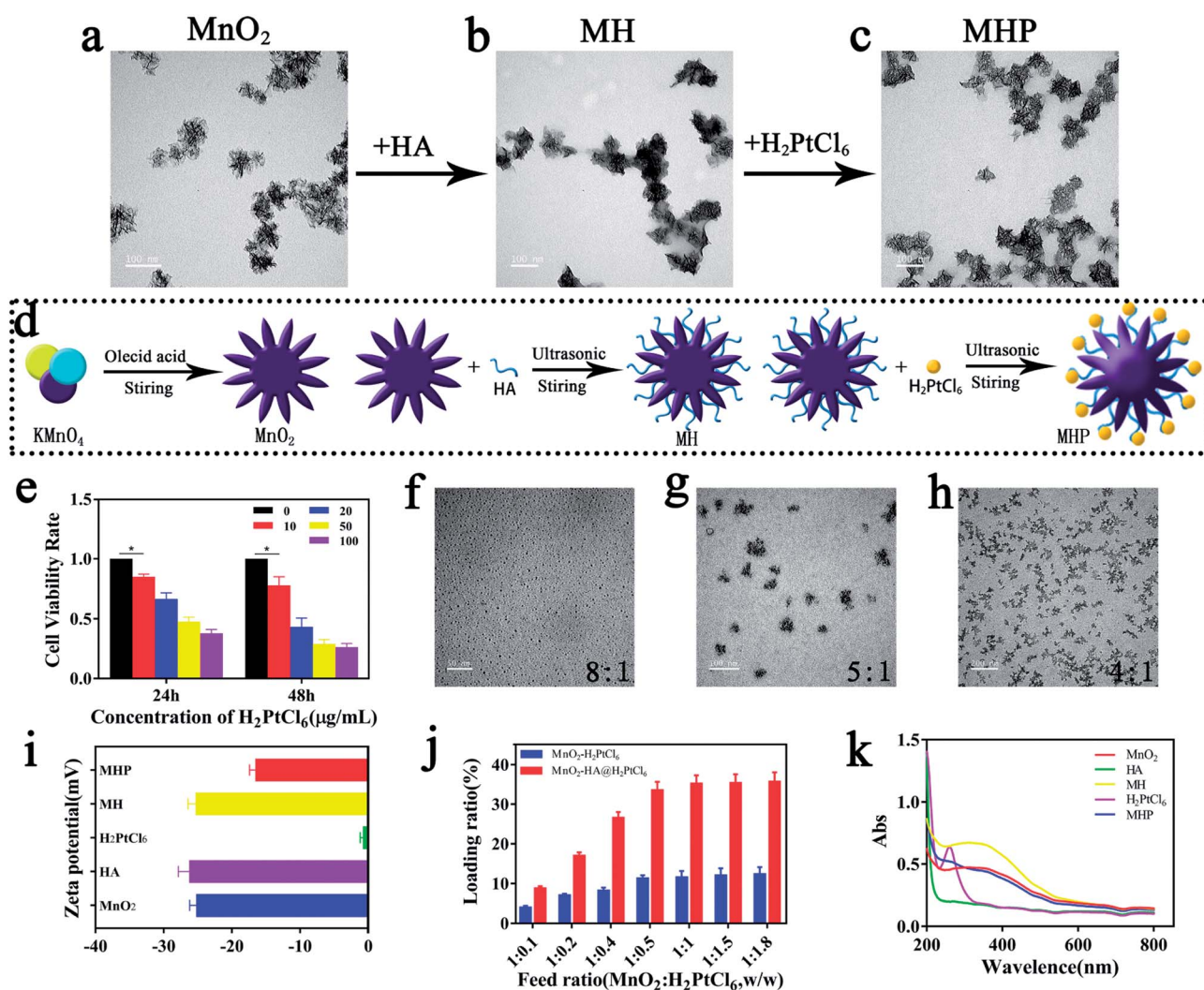


Fig. 1 (a) TEM image of  $\text{MnO}_2$  NPs, scale bar: 100 nm; (b) TEM image of  $\text{MnO}_2\text{-HA}$ , scale bar: 100 nm; (c) TEM image of  $\text{MnO}_2\text{-HA@H}_2\text{PtCl}_6$ , scale bar: 100 nm; (d) schematic illustration of synthesis of MHP; (e) HCT-116 cell viabilities after incubation with  $\text{H}_2\text{PtCl}_6$  for 24 and 48 h; (f–h) TEM images of  $\text{HA-H}_2\text{PtCl}_6$  at different ratios of  $\text{HA/H}_2\text{PtCl}_6$ . The scales are 50, 100, and 200 nm, respectively; (i) zeta potential of  $\text{MnO}_2$ , HA,  $\text{H}_2\text{PtCl}_6$ , MH, and MHP; (j) loading efficiency of  $\text{H}_2\text{PtCl}_6$  at different ratios; (k) UV-Vis-NIR of  $\text{MnO}_2$ , HA,  $\text{H}_2\text{PtCl}_6$ , MH, and MHP. \* $P < 0.05$ .



treatment with  $20 \mu\text{g mL}^{-1}$   $\text{H}_2\text{PtCl}_6$  for 8 h could cause cell apoptosis by around 81% (Fig. S2†), in addition to remarkable double-strand breaks in DNA (Fig. S3†). *In vitro*, different ratios of  $\text{HA}/\text{H}_2\text{PtCl}_6$  might form nanoparticles with different sizes. When the mass ratio turns out to be 8 : 1, 5 : 1, and 4 : 1, the particle size is less than 50 nm (Fig. 1b–d). Moreover, when the proportion of  $\text{H}_2\text{PtCl}_6$  is excessive (Fig. S4†), a ratio of 1 : 5 seems to be appropriate to form regular nanoparticles; when the ratio is 1 : 4, regular nanoparticles cannot be formed; however, when the ratio is 1 : 8, the proportion of  $\text{H}_2\text{PtCl}_6$  may be excessive. Hence, we can speculate that the binding of HA to  $\text{H}_2\text{PtCl}_6$  may be based on the chelation of the Pt-centered atom and HA-ligand.

Eventually,  $\text{H}_2\text{PtCl}_6$  was added to the surface of MH to form  $\text{MnO}_2\text{-HA@H}_2\text{PtCl}_6$  (MHP). With the help of inductively coupled plasma mass spectrometry (ICP-MS), it was revealed that the drug-loading efficiency of  $\text{H}_2\text{PtCl}_6$  was increased with the increase of  $\text{H}_2\text{PtCl}_6$ , and this may be due to high specific surface area of  $\text{MnO}_2$ . Furthermore, when HA was used as the medium, the drug-loading efficiency of  $\text{H}_2\text{PtCl}_6$  was

significantly increased, which was about 35% when  $\text{MnO}_2\text{:HA:H}_2\text{PtCl}_6 = 1:20:1$  (w:w:w, Fig. 1j). As shown in Fig. 1c, the particle size was mainly distributed in the range of 80–120 nm (average size: 100 nm) by dynamic light scattering (DLS) (Fig. 2b). Zeta potential showed that the reduction of negative surface charge was associated with loading of  $\text{H}_2\text{PtCl}_6$  (Fig. 1i), which may due to the combination of  $\text{H}^+$  with the carboxylate of HA. The successful synthesis of MHP was verified by ultraviolet-visible-near infrared (UV-Vis-NIR) spectroscopy (Fig. 1k) and energy dispersive X-ray spectroscopy (EDS) (Fig. S5†).

## 2.2 Properties of MHP

The TME has a higher amount of  $\text{H}_2\text{O}_2$  ( $\sim 100 \mu\text{M}$ ) and acidic environment,<sup>17–20</sup> in which MHP can immediately produce a great number of air bubbles, indicating that  $\text{O}_2$  was produced rapidly, and simultaneous production of  $\text{Mn}^{2+}$  which is a strong magnetic resonance imaging (MRI) contrast agent. TEM and DLS showed that MHP could release USNPs ( $\sim 20$  nm) during 30 min (Fig. 2a and b), and the TEM image of that incubated

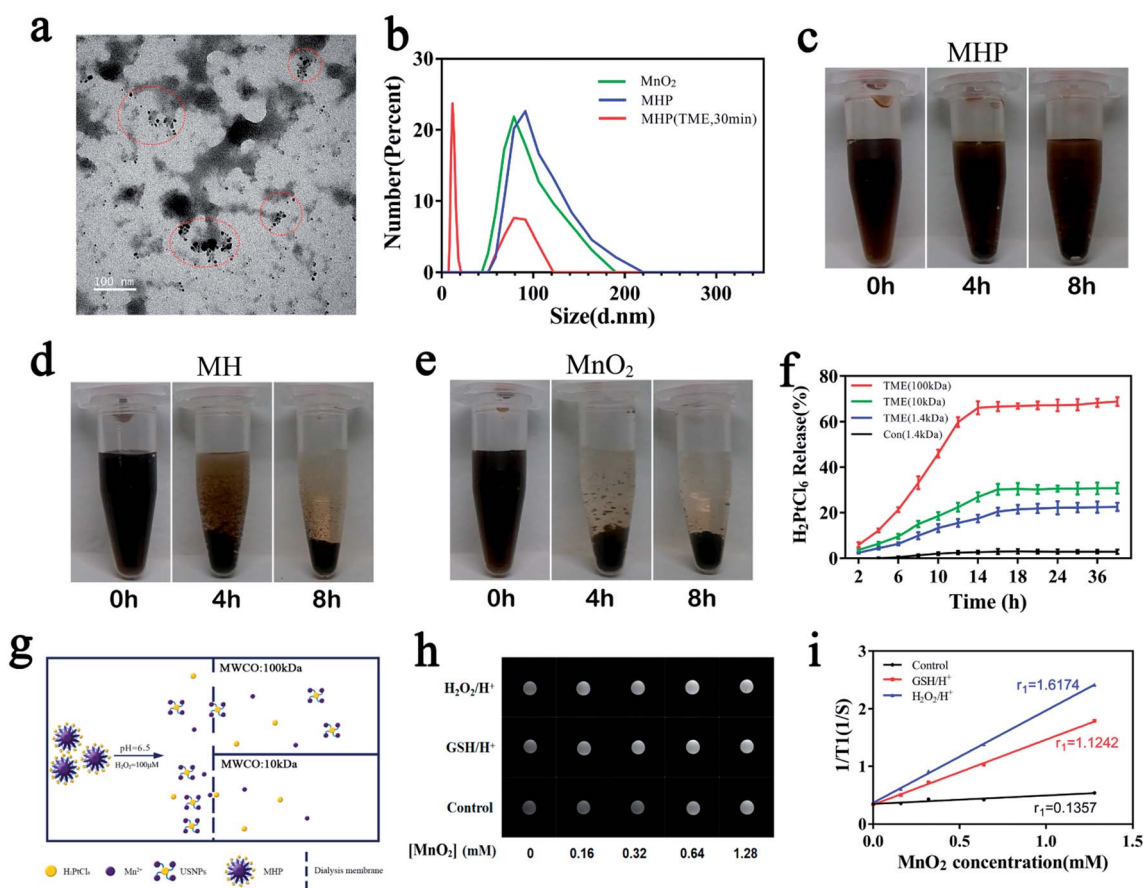


Fig. 2 (a) TEM image and (b) DLS analysis of MHP after incubation in saline at  $\text{H}_2\text{O}_2 = 100 \mu\text{M}/\text{pH} = 6.5$  for 30 min; (c–e) appearance of MHP, MH, and  $\text{MnO}_2$  dispersed in saline at 0, 4, and 8 h, respectively. (f) Cumulative  $\text{H}_2\text{PtCl}_6$  release of MHP under different conditions *via* dialysis with molecular weights of 1.4, 10, and 100 kDa, respectively. (TME:  $\text{H}_2\text{O}_2 = 100 \mu\text{M}/\text{pH} = 6.5$ , control:  $\text{H}_2\text{O}_2 = 0 \mu\text{M}/\text{pH} = 7.4$ ); (g) USNPs were released from MHP in the TME, and then passed through the dialysis membranes with a molecular weight of 100 kDa, while dialysis membranes with a molecular weight of 10 kDa only allowed  $\text{Mn}^{2+}$  and  $\text{H}_2\text{PtCl}_6$  to pass through; (h)  $T_1$ -weighted magnetic resonance imaging (MRI) of MHP, MHP +  $\text{GSH}/\text{H}^+$ , and MHP +  $\text{H}_2\text{O}_2/\text{H}^+$ ; (i) MRI of the MHP:  $1/T_1$  versus  $\text{MnO}_2$  concentration for MHP, the MHP +  $\text{GSH}/\text{H}^+$ , and MHP +  $\text{H}_2\text{O}_2/\text{H}^+$ .



overnight is shown in Fig. S6.† Centrifugation at 16 000 rpm for 10 min and dialysis (14 000 MW) were carried out, and ICP-MS demonstrated  $[Mn] : [Pt]$  in the supernatant before dialysis, in the supernatant after dialysis, and precipitation after dialysis, which were (1.27097–1.28031), (1.15368–1.16724), and (1.16223–1.16856), respectively. However,  $[Mn] : [Pt]$  was approximately equal to 3.772 in MHP, which showed the release of superfluous  $Mn^{2+}$  during transformation. The UV-Vis-NIR did not show the absorption peak of HA in the supernatant after dialysis, suggesting that HA was approximately 100% transformed. Therefore, we can preliminarily speculate that the chemical formula of the USNPs is as follows:  $(Mn)_{4n} (H_2PtCl_6)_n (C_{14}H_{20}NO_{11}Na)_x$ , which may be formed by the self-assembly of  $Mn^{2+}$ , HA, and  $H_2PtCl_6$ .

Next, the stability of the NPs was tested with saline. It was observed that  $MnO_2$  was almost fully aggregated and precipitated during 4 h (Fig. 2e), reflecting a poor hydrodynamic stability, which is consistent with findings of a previous study.<sup>21</sup> Importantly, MH showed a large amount of precipitation, while MHP revealed nearly no precipitation during 4 h (Fig. 2c and d); after 8 h, MH was almost fully precipitated, whereas MHP only revealed a small amount of precipitation, demonstrating that MHP had superior stability to  $MnO_2$  and MH in saline, and this may be related to the surface charge and dispersion of NPs. Although it was disclosed that the hydrodynamic stability of

$MnO_2$  NPs has been improved after modifying the HA surface, there are a number of defects in the present study related to a nano-integrated platform, and MHP can be therefore utilized as an alternative.

The ability of MHP to release  $H_2PtCl_6$  in the TME was examined by ICP-MS (Fig. 2f). The release of  $H_2PtCl_6$  was nearly undetectable in a control environment (pH = 7.4,  $H_2O_2$  = 0  $\mu M$ , MWCO: 1.4 kDa), which showed an appropriate integrity of MHP. Small amounts of  $H_2PtCl_6$  were released in the TME (pH = 6.5,  $H_2O_2$  = 100  $\mu M$ , MWCO = 1.4 kDa), demonstrating that MHP had satisfactory oxidation–reduction reactions. Distinct  $H_2PtCl_6$  released profiles were obtained by dialysis at different molecular weight cut-off values (10k, 100k); thus, we postulated that MHP could partially disassemble into USNPs (~20 nm) in saline in the TME (Fig. 2g).

It is noteworthy that  $Mn^{2+}$  released from  $MnO_2$  into the TME is an efficient MRI contrast agent.<sup>22,23</sup> MRI was applied for diagnosis of tumors with a 1.5 T clinical MR scanner at room temperature. Images of the three groups showed different degrees of whitening effects with the increase of the  $MnO_2$  concentration (Fig. 2h). The  $r_1$  values after the reaction under glutathione (GSH) (2 Mm, pH 5.0) or  $H_2O_2$  (100  $\mu M$ , pH 5.0) for 6 h were 1.1242 and 1.6174  $mM^{-1} s^{-1}$ , respectively (Fig. 2i), which were 8.28 times (1.1242/0.1357) and 11.9 times (1.6174/0.1357) higher than those in the control group. This indicates that MHP

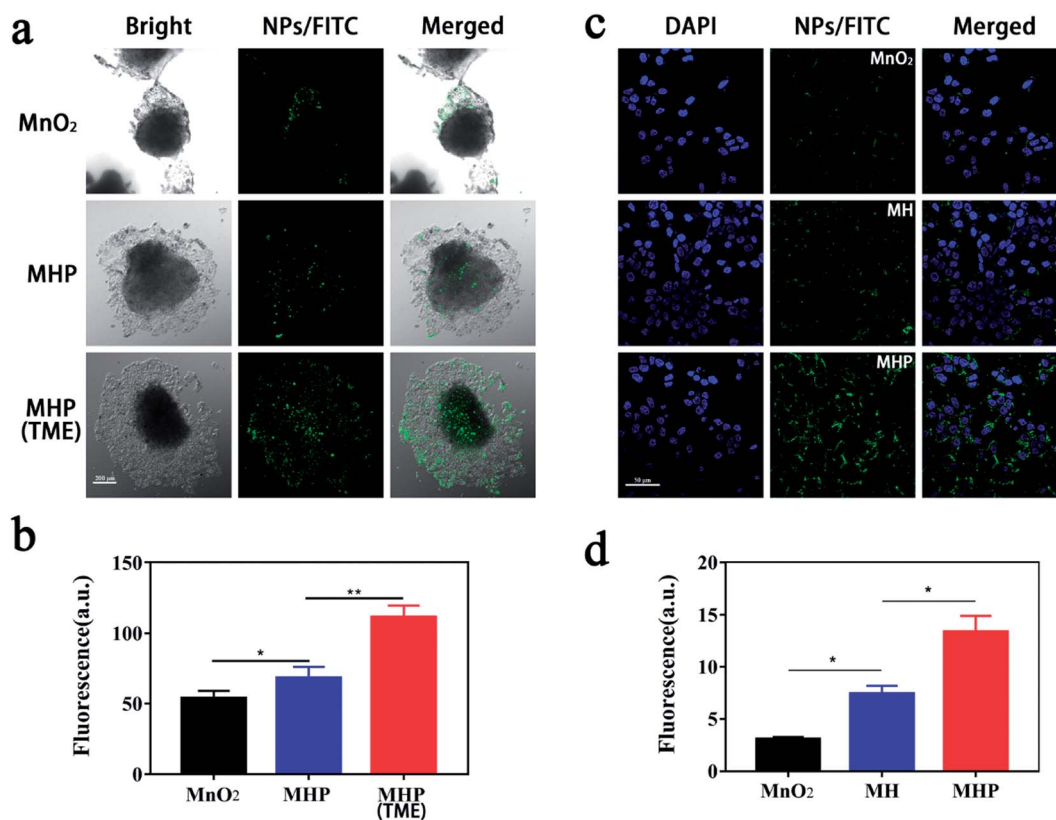


Fig. 3 (a) *In vitro* penetration and (b) quantitative detection of NPs in HCT-116 multicellular spheroids (MCSs) 6 h post-incubation in saline under different conditions. Green represents FITC-labeled NPs. Scale bar: 200  $\mu m$ ; (c) NPs were absorbed or associated with cell membranes. Green represents FITC-labeled NPs and blue represents DAPI. Scale bar: 50  $\mu m$ ; (d) quantitative detection of NPs at 6 h after incubation with HCT-116 cells. \* $P < 0.05$ ; \*\* $P < 0.01$ .



has a strong T1 imaging function in the TME, and that it is feasible as a positive MRI contrast agent.

### 2.3 *In vitro* penetration ability and cellular uptake test

In this stage, a multicellular sphere (MCS) model was used to assess the *in vitro* penetration ability of MHP. We incubated equivalent fluorescein-5-isothiocyanate (FITC)-labeled NPs with MCS under different conditions for 6 h, and their penetration depth was measured by confocal laser scanning microscopy (CLSM) (Fig. 3a). Compared with the MnO<sub>2</sub> group, whose green fluorescence only appeared in small amounts of cells outside the sphere, fluorescence was slightly observed both inside and around the cell sphere in the MHP group. The cellular uptake test showed that NPs absorbed by HCT-116 cells or associated

with cell membranes were MHP/FITC, MH/FITC, and MnO<sub>2</sub>/FITC, which ranked from maximum to minimum (Fig. 3c and d). This may be due to the hierarchical dispersion of NPs and CD44 receptors' targeting effect of HA.<sup>24,25</sup> Importantly, fluorescence in the MCS was the strongest in all groups when incubated in the TME (H<sub>2</sub>O<sub>2</sub> = 100 μM/pH = 6.5) (Fig. 3b), which further indicated that MHP released USNPs under the circumstance of the TME.

### 2.4 Cytotoxicity assay

We evaluated the *in vitro* cytotoxicity of MH, H<sub>2</sub>PtCl<sub>6</sub>, and MHP combined with radiation (Fig. 4a). Before any treatment, a small amount of sterile paraffin was covered on the surface of the cell culture medium to simulate the hypoxic environment of

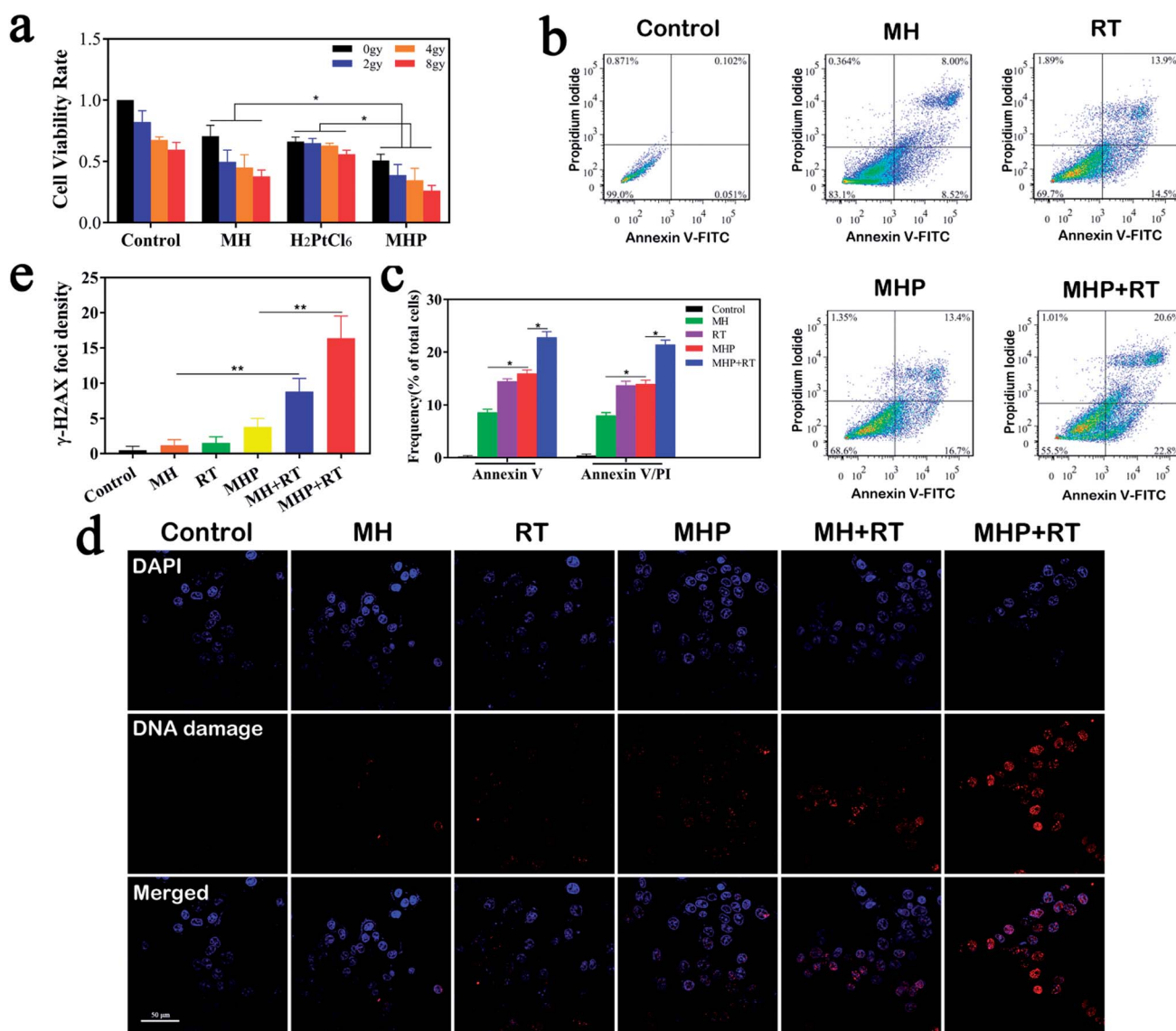


Fig. 4 (a) Cytotoxicity of HCT-116 cells treated with MH, H<sub>2</sub>PtCl<sub>6</sub>, and MHP (MnO<sub>2</sub>/H<sub>2</sub>PtCl<sub>6</sub> = 50/17.5 μg mL<sup>-1</sup>) at different radiation doses at 0, 2, 4, and 8 Gy; (b) flow cytometry analysis; (c) quantitative analysis of apoptosis induced by MH or MHP (MnO<sub>2</sub>/H<sub>2</sub>PtCl<sub>6</sub> = 50/17.5 μg mL<sup>-1</sup>) combined with or without radiation (5 Gy); (d) immunofluorescence staining of γ-H2AX foci in HCT-116 cells treated with saline, MH, and MHP (MnO<sub>2</sub>/H<sub>2</sub>PtCl<sub>6</sub> = 50/17.5 μg mL<sup>-1</sup>), with or without radiation (5 Gy). Blue represents DAPI and red represents Cy3 double-strand breaks in DNA. Scale bar: 50 μm; (e) quantitative analysis of γ-H2AX foci (γ-H2AX foci/100 μm<sup>2</sup>) for *n* > 100 cells in each treatment group. \**P* < 0.05; \*\**P* < 0.01.



tumors. The results showed that the cell proliferation rate gradually decreased in all the groups with the increase of irradiation dose. Additionally, MHP with the same radiation dose had the strongest inhibition rate in all the groups, which demonstrated the necessity of MH for loading  $H_2PtCl_6$ , laying a foundation for clinical application and transformation. It may be related to the following factors: (1)  $MnO_2$  had the effect of radio-sensitization. (2) HA had the function of transforming M2 phenotype TAMs into M1 phenotype TAMs, thereby reducing the resistance of tumors to chemotherapy.<sup>14</sup> (3) MHP was more susceptible to be absorbed or associated with cell membranes.

We then assessed whether MH-loaded  $H_2PtCl_6$  increased the apoptosis-inducing effect on HCT-116 cells (Fig. 4b and c). The findings manifested that MH can slightly induce cell apoptosis. Whether early or late apoptosis, the proportion of cells induced by MHP was similar to that of radiation (5 Gy), while being greater than that of MH. Moreover, MHP combined with radiation induced the largest proportion of apoptotic cells in all the groups. Therefore, we speculated that the apoptotic induction of MHP may be one of the reasons for its cytotoxicity.

Several studies have shown that  $MnO_2$  can consume endogenous  $H_2O_2$  in the TME<sup>26–29</sup> and consistently produce oxygen to overcome hypoxic environments, and also attenuate the resistance of radio-chemotherapy.<sup>30–32</sup> In the present study, Cy3-labeled  $\gamma$ -H2AX antibody was used to reflect double-strand breaks in DNA (Fig. 4d). Different groups, including control, MH, RT alone, and MHP, showed no obvious DNA breaks. Compared with the MH or MHP group, the MH + RT group and MHP + RT group had a significantly higher percentage of cells with DNA strand breaking (Fig. 4e), indicating that both MH and MHP had satisfactory radio-sensitization.

## 2.5 *In vivo* MRI and fluorescence (FL) imaging

Given their biodegradability and  $T_1$ -weighted MRI capabilities,  $MnO_2$  NPs were chosen as the carriers of a nano-integrated diagnostic and therapeutic platform. HCT-116-tumor-bearing mice were injected with MHP nanoparticles ( $5\text{ mg kg}^{-1}$ ) through their tail vein. Then,  $T_1$ -weighted MRI images were acquired at different time points (Fig. 5a). The signal intensity of both groups similarly showed upward, downward, and slow

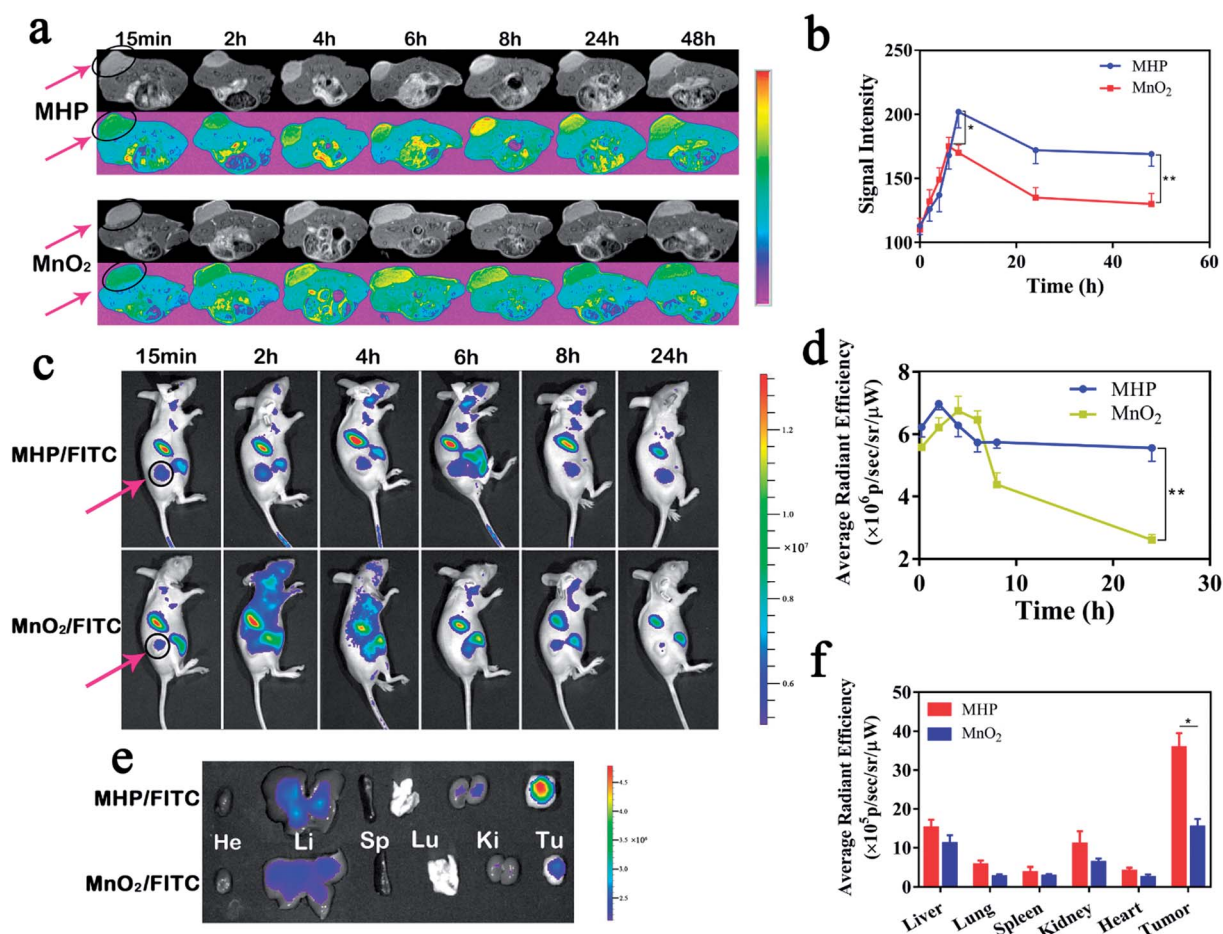


Fig. 5 (a)  $T_1$ -weighted MR images; (b) MR signal intensities of tumors (black circles) in mice injected with  $5\text{ mg kg}^{-1}$  MHP or  $MnO_2$  *via* tail veins,  $n = 3$ ; (c) fluorescence (FL) imaging; (d) average radiant efficiency in tumors (black circles) calculated at different time points after *i.v.* injection of MHP/Cy5.5 or  $MnO_2$ /Cy5.5 in HCT-116 tumor-bearing mice,  $n = 3$ ; (e) FL imaging; (f) average radiant efficiency in vital organs of mice and tumors at 48 h following MHP/Cy5.5 or  $MnO_2$ /Cy5.5 treatment (He: Heart, Li: Liver, Sp: Spleen, Lu: Lung, Ki: Kidney, Tu: Tumor),  $n = 3$ . \* $P < 0.05$ ; \*\* $P < 0.01$ .



decline trends, while the peak value and the steady-state value after 48 h in the MHP group were higher than those in the  $\text{MnO}_2$  group. Afterwards, MHP and  $\text{MnO}_2$  were labeled with equivalent Cy5.5, and the metabolism and distribution of MHP and  $\text{MnO}_2$  in mice were determined by FL imaging (Fig. 5c). Within 24 h, the average radiant efficiency in the MHP group was notably higher than that in the  $\text{MnO}_2$  group (Fig. 5d). The mice were sacrificed after 48 h and the tumors and organs were removed (Fig. 5e), in which the retention of MHP in tumors was higher than that of  $\text{MnO}_2$ , and there was no significant difference between them in the main organs (Fig. 5f). On the one hand, the EPR effect of MHP was found to be stronger than that of  $\text{MnO}_2$  NPs, which might be related to the superior hydrodynamic stability of MHP, and HA also played a substantial role in tumor binding *in vivo*. On the other hand, due to the metabolic properties of MHP, the accumulation in the main organs was limited.

## 2.6 *In vivo* penetration and combination therapy

In addition to using the MCS to study the penetration of NPs, we also assessed *in vivo* penetration by co-localization percentage of a vascular marker, namely CD31 (red) and FITC-labeled NPs (green). Moreover,  $\text{MnO}_2$  NPs/FITC and MHP/FITC ( $5 \text{ mg kg}^{-1}$ )

were injected into tumor-bearing mice *via* the tail vein, and tumor tissues were collected after 24 h, and then frozen tissue sections were examined by CLSM (Fig. 6a). In the MHP group, there was less co-localization between NPs and blood vessels, while more yellow appeared in the  $\text{MnO}_2$  group. On the one hand, it was revealed that  $\text{MnO}_2$  NPs had limited penetration ability because of their large particle size and physical properties and could easily aggregate and precipitate, and the majority of them remained on the vascular wall. On the other hand, due to oxidation–reduction reactions of MHP in the TME, once the tumors were entered, MHP released USNPs ( $\sim 20 \text{ nm}$ ), which resulted in an excellent interstitial penetration.

As MRI and FL imaging *in vivo* showed that MHP had a promising EPR influence, we further studied the anti-cancer effect of MHP combined with radiotherapy *in vivo*. MH and MHP ( $5 \text{ mg kg}^{-1}$ ) were injected into HCT-116-tumor-bearing mice *via* the tail vein. After 8 h, 5 Gy radiation was carried out on the tumor site. After this, the volume of tumors was monitored every other day for 14 days (Fig. 6c). The mice in the control group grew faster, and the volume of tumors in the mice on the 14th day was about 9 times higher than that at the beginning. The MHP + RT group (about 1.07 times) showed the best tumor

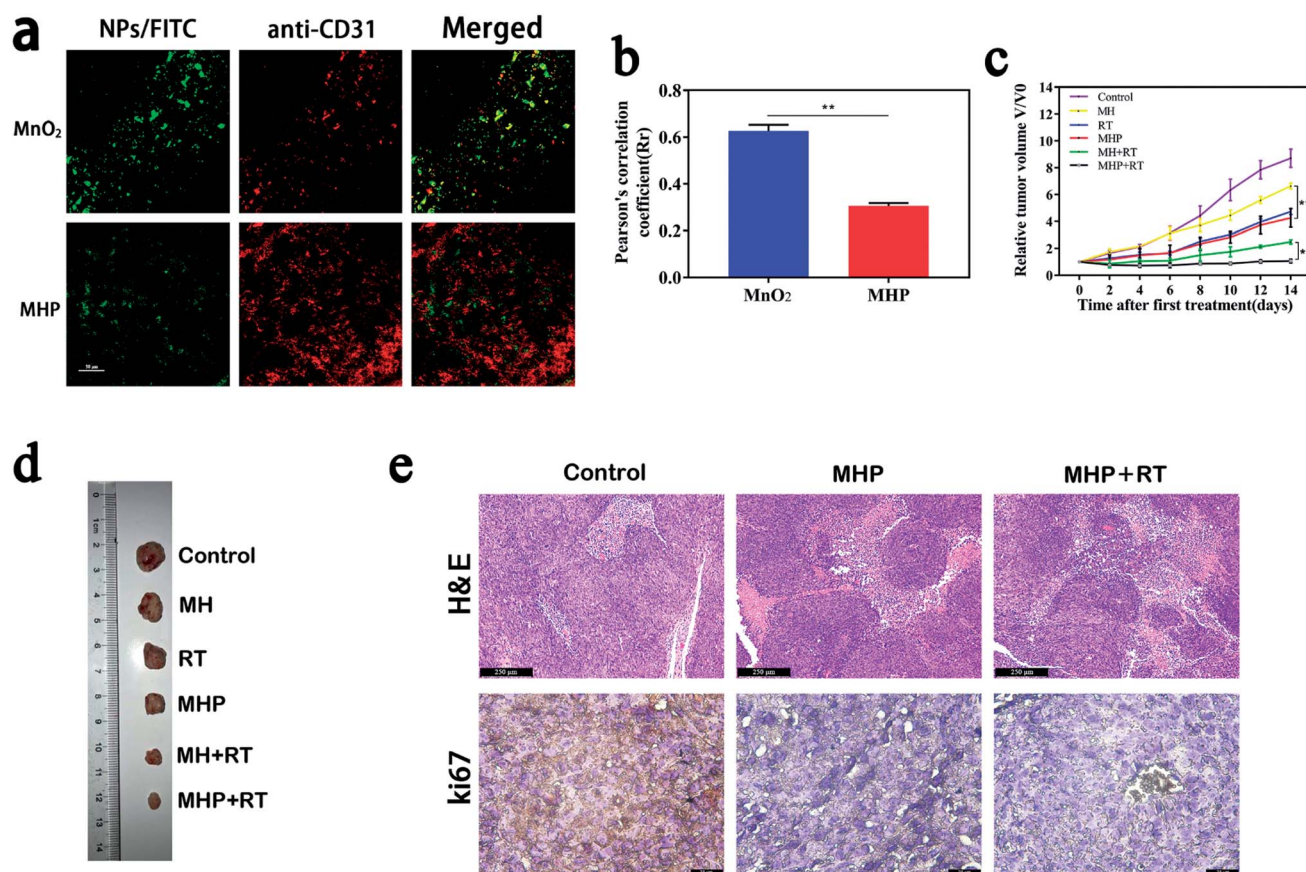


Fig. 6 (a) Confocal images of tumor slices dissected from mice at 24 h post *i.v.* injection of  $\text{MnO}_2$  or MHP. Blue and red signals represent NPs and anti-CD31-stained blood vessels, respectively. Scale bar:  $50 \mu\text{m}$ ; (b) the Pearson correlation coefficient ( $R_r$ ) calculated in the image, as shown in (a); (c) tumor growth,  $n = 5$ ; (d) representative tumor images on day 14th; (e) images of hematoxylin and eosin (H & E) staining and Ki67 immunohistochemical staining on the 3rd day post therapy. Scale bar:  $250 \mu\text{m}$  (H & E);  $25 \mu\text{m}$  (Ki67). \* $P < 0.05$ ; \*\* $P < 0.01$ .



suppression effect. Fig. 6d illustrates tumor entities in each treatment group obtained on the 14th day.

To further perceive the inhibitory influence of MHP combined with radiotherapy on tumor growth, hematoxylin and eosin (H & E) staining and Ki67 immunohistochemistry (Fig. 6e) were carried out in tumor tissues on the 2nd day after treatment, and it was revealed that distinct tissue necrosis and Ki67 expression decreased in both the MHP group and MHP + RT group.

### 2.7 Blood testing and histological examinations

There was no aberration in mice during the entire post-treatment period. Although a small amount of MHP was accumulated in the liver and kidneys after injection *via* the tail vein, the targets of the blood routine and blood biochemical values on the 1st and 7th days after treatment are shown in Fig. 7a. Besides, the white blood cell (WBC), red blood cell (RBC), hemoglobin (HGB), platelet count (PLT), alanine aminotransferase (ALT), aspartate aminotransferase (AST), blood urea nitrogen (BUN), creatinine (CREA), mean corpuscular hemoglobin concentration (MCHC), hematocrit (HCT), mean corpuscular volume (MCV), mean corpuscular hemoglobin (MCH), mean platelet volume (MPV), and platelet distribution width (PDW) showed no significant difference compared with the control group. Additionally, 48 h post-treatment, H & E staining of the main organs of the mice showed no significant

damage compared with the control group (Fig. 7b). Mice treated with radiotherapy slightly lost weight at the beginning, but recovered rapidly later (Fig. 7c). These results demonstrated that MHP may be a relatively safe nano-drug in the short term, and further in-depth toxicity assessments should be carried out in the future.

## 3 Experimental testing

### 3.1 Materials

HA (10 K) was purchased from Lifecore Biomedical LLC (Chaska, MN, USA);  $\text{H}_2\text{PtCl}_6 \cdot 6\text{H}_2\text{O}$  was provided by Macklin (Shanghai, China); Cy5.5 was purchased from Meilunbio (Dalian, China). Moreover, a cell counting kit-8 (CCK-8) was purchased from Dojindo Molecular Technologies, Inc. (Kumamoto, Japan);  $\gamma\text{-H2AX}$  human anti-rabbit antibody was provided by Arigo Biolaboratories Inc. (Hsinchu, Taiwan); an Annexin V-FITC/PI apoptosis assay kit was purchased from TransDetect (Beijing, China); and Ki67 human anti-rabbit antibody was provided by Affinity Inc. (New York, NY, USA).

### 3.2 Synthesis and characterization of $\text{MnO}_2$ NPs

The synthesis of  $\text{MnO}_2$  NPs was conducted as previously described, which was slightly modified accordingly.<sup>33</sup> Firstly, 0.1 g  $\text{KMnO}_4$  was added to 50 mL ultra-pure water and stirred for 10 min to be fully dissolved. Furthermore, 35  $\mu\text{L}$  oleic acid was

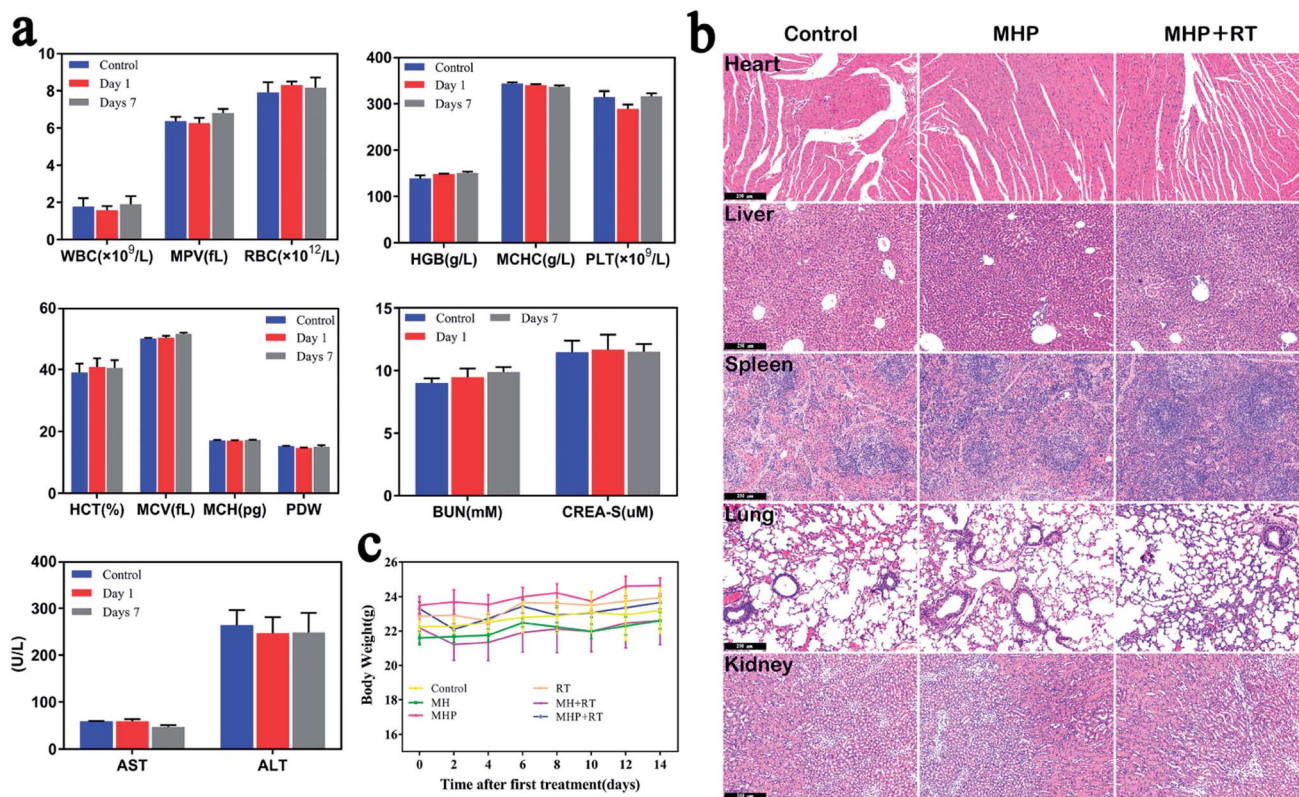


Fig. 7 (a) Blood routine and biochemical tests on the 1st and 7th days after i.v. injection of MHP ( $5 \text{ mg kg}^{-1}$ ) in female nude mice,  $n = 5$ ; (b) H & E staining images of major organs (heart, liver, spleen, lungs, and kidneys) at 48 h after i.v. injection of MHP or MHP + RT ( $5 \text{ mg kg}^{-1}$ , 5 Gy). Scale bar: 250  $\mu\text{m}$ ; (c) body weight monitoring of HCT-116-tumor-bearing mice every other day post-treatment,  $n = 5$ .





added to the solution and stirred for 20 h at room temperature. The color of the solution changed from dark purple to brown black, suggesting that  $\text{Mn}^{7+}$  was reduced to  $\text{Mn}^{4+}$ . The colloidal solution was centrifuged for 8 min at room temperature at 8000 rpm; the supernatant was taken and centrifuged for 8 min at 15 000 rpm, and the precipitate was taken and washed five times with 75% ethanol using ultrasonication. Finally, at a constant temperature of 60 °C, TEM, EDS, UV-Vis-NIR, and DLS (Malvern) were utilized for detection.

### 3.3 Synthesis and characterization of $\text{MnO}_2$ -HA (MH) and $\text{MnO}_2$ -HA@ $\text{H}_2\text{PtCl}_6$ (MHP)

Synthesis of MH and MHP was performed based on the layer-by-layer (LBL) method. For this purpose, firstly, the pre-synthesized  $\text{MnO}_2$  NPs were added to a certain amount of ultra-pure water and treated using an ultrasonic cell breaker (amplitude: 35%) for 30 s  $\times$  5 times. Secondly, HA and chloroplatinic acid with a certain mass ratio were added; the colloidal solution was subjected to ultrasonication 30 s  $\times$  3 times under the same conditions, and stirred for 8 h. Afterwards, it was centrifuged at 15 000 rpm for 8 min to obtain a precipitate. Finally, this was washed with ultra-pure water and dried at a constant temperature of 60 °C to achieve MH and MHP. TEM, DLS, ICP-MS and UV-Vis-NIR were used for detection as well.

### 3.4 Cellular experiments

To explore the ability of MHP to penetrate into tumors, we produced HCT-116 multicellular spheres.<sup>34,35</sup> Briefly, the bottom of a 6-well plate was covered with 0.5 mL agarose liquid (1.5 w/v%), after being cooled at room temperature, and a layer of agarosepectin was formed on its surface. Then,  $3 \times 10^5$  HCT-116 cells and medium were co-incubated in each well for about 12 days, in which the suspension was mixed with 1 mL pipettes every 3 days. The same amount of FITC-labeled NPs ( $20 \mu\text{g mL}^{-1}$  of  $\text{MnO}_2$ ) was added to the approximate equal amount of multicellular spheres for 6 h. Additionally, HCl and  $\text{H}_2\text{O}_2$  were used to adjust the experimental conditions. The CLSM was used to observe the results. Cellular uptake was herein conducted as follows:  $3 \times 10^5$  HCT-116 cells were seeded in a glass-bottom culture dish.  $\text{MnO}_2$  NPs/FITC, MH/FITC, and MHP/FITC ( $20 \mu\text{g mL}^{-1}$  of  $\text{MnO}_2$ ) were incubated for 6 h. Green represents FITC-labeled NPs and blue represents the nucleus. Then, the findings were observed with a laser confocal microscope. Cytotoxicity assay:  $3 \times 10^3$  HCT-116 cells were seeded into 96-well plates and incubated for 24 h. Micro-amounts of sterile paraffin were used to cover the surface of the culture medium for 12 h in order to provide an appropriate hypoxic environment. Afterwards, MH,  $\text{H}_2\text{PtCl}_6$ , and MHP ( $\text{MnO}_2/\text{H}_2\text{PtCl}_6 = 50/17.5 \mu\text{g mL}^{-1}$ ) were added to the culture medium in the presence of paraffin, respectively. After 12 h, 0/2/4/8 Gy of radiation were given, the old medium was removed from the 96-well plate, and fresh medium was added for another 72 h. Relative cell viabilities were analyzed by the CCK-8 assay. Detection of double-strand breaks in DNA was performed as well: MH,  $\text{H}_2\text{PtCl}_6$ , and MHP ( $\text{MnO}_2/\text{H}_2\text{PtCl}_6 = 50/17.5 \mu\text{g mL}^{-1}$ ) were added into a glass-bottom culture dish containing pre-seeded HCT-116 cells.

Radiation (5 Gy) was given after incubation for 8 h. Then, incubation was followed for another 30 min. Red represents Cy3 labeled double-strand breaks in DNA, and blue represents DAPI. A laser confocal microscope was utilized for visualization.

### 3.5 *In vivo* MR and FL imaging

All animals were purchased from the Animal Experimental Center of Xiamen University (Xiamen, China) and were used in accordance with the Institutional Animal Care and Use Committee (IACUC) and approved by the Ethics Committee of the Xiamen University. Moreover,  $5 \times 10^6$  HCT-116 cells mixed with Matrigel were subcutaneously injected into female BALB/c nude mice. For FL imaging,  $\text{MnO}_2/\text{Cy5.5}$  and MHP/Cy5.5 ( $5 \text{ mg kg}^{-1}$ ) were injected into HCT-116-tumor-bearing mice ( $300\text{--}350 \text{ mm}^3$ ) *via* the tail vein. These mice were scanned with an optical imaging system (IVIS Lumina II) at intervals and were executed at 48 h, after which their tumors and main organs were used for FL imaging. For *in vitro* MRI, MHP solutions with different  $\text{MnO}_2$  concentrations treated with or without  $\text{H}_2\text{O}_2/\text{GSH}$  under acidic conditions were scanned using a 1.5 T clinical MR scanner at room temperature. The relaxation rate  $r_1(1/T_1)$  was accordingly calculated. For *in vivo* MRI,  $\text{MnO}_2$  NPs and MHP ( $5 \text{ mg kg}^{-1}$ ) were injected into HCT-116-tumor-bearing mice ( $300\text{--}350 \text{ mm}^3$ ) *via* the tail vein. A MRI instrument (9.4 T; Bruker Corp., Billerica, MA, USA) was used for monitoring as well.

### 3.6 *In vivo* penetration

HCT-116 tumor-bearing mice ( $300\text{--}350 \text{ mm}^3$ ) were injected with  $\text{MnO}_2$  NPs/FITC and MHP/FITC ( $5 \text{ mg kg}^{-1}$ ) through the tail vein, respectively. These mice were executed after 24 h. Tumor tissues were frozen and sliced. Red represents Alexa Fluor 488-labeled CD31 antibody and green represents FITC-labeled NPs. A laser confocal microscope was then utilized for visualization.

### 3.7 *In vivo* combined therapy

HCT-116 tumor-bearing mice ( $100 \text{ mm}^3$ ) were randomly divided into 6 groups ( $n = 5$ ). Besides, MH and MHP ( $5 \text{ mg kg}^{-1}$ ) were injected into the tail vein, respectively. After 8 h, covering the area with a lead plate except the tumor, mice underwent radiation at a dose of 5 Gy. The volume of tumor ( $V = \text{length} \times \text{width}^2/2$ ) and body weight of these mice were recorded by every other day post-treatment for 2 weeks. Then, those mice were executed on the 14th day, and the tumors of the mice were taken out and photographed. Another array of tumor-bearing mice were executed 48 h after treatment. Furthermore, H & E staining and Ki67 immunohistochemical staining were performed.

### 3.8 Blood testing and histological examinations

Female-nude mice received the same amount of saline and MHP ( $5 \text{ mg kg}^{-1}$ ) through the tail vein. The values of routine blood and blood biochemical tests were detected after 24 h and on the 7th day, respectively (WBC, RBC, HGB, PLT, ALT, AST, BUN, CREA-S, MCHC, HCT, MCV, MCH, MPV, and PDW). Another array of female tumor-bearing mice received saline and MHP ( $5 \text{ mg kg}^{-1}$ ) through the tail vein. Combined with



radiation (5 Gy), these mice were executed at 48 h post-treatment, and major organs (*e.g.*, heart, liver, spleen, lung, kidney) were taken out to carry out H & E staining.

## 4 Conclusions

In the present study, we synthesized short-term biosafety MHP as an ultra-small NP (USNP) generator by electrostatic adsorption between MnO<sub>2</sub> NPs and HA, and the chelation between HA and H<sub>2</sub>PtCl<sub>6</sub>. The maximum loading efficiency of H<sub>2</sub>PtCl<sub>6</sub> reached 35%. Saline stable MHP with an appropriate initial size (average: 100 nm) was highly aggregated at the tumor site through the EPR effect and HA targeting, stayed longer, in response to acidic and relatively high H<sub>2</sub>O<sub>2</sub> TME conditions, and was rapidly decomposed into numerous USNPs (~20 nm) through supramolecular self-assembly of Mn<sup>2+</sup>, HA, and H<sub>2</sub>PtCl<sub>6</sub>. Then we preliminarily speculated the chemical formula of USNP: (Mn)<sub>4n</sub>(H<sub>2</sub>PtCl<sub>6</sub>)<sub>n</sub>(C<sub>14</sub>H<sub>20</sub>NO<sub>11</sub>Na)<sub>x</sub>. So, MHP could uniformly penetrate into MCSs and solid tumors, and was more conducive to radio-chemotherapy. It also has biodegradability and bioimaging functions that allow use of MRI to monitor drug delivery and scientific radiotherapy program adjustment.

## Conflicts of interest

There are no conflicts to declare.

## References

- 1 P. Wardman, Chemical radiosensitizers for use in radiotherapy, *Clin. Oncol.*, 2007, **19**(6), 397–417.
- 2 L. Tang, X. Yang, Q. Yin, K. Cai, H. Wang, I. Chaudhury, C. Yao, Q. Zhou, M. Kwon, J. A. Hartman, I. T. Dobrucki, L. W. Dobrucki, L. B. Borst, S. Lezmi, W. G. Helderich, A. L. Ferguson, T. M. Fan and J. Cheng, Investigating the optimal size of anticancer nanomedicine, *Proc. Natl. Acad. Sci. U. S. A.*, 2014, **111**(43), 15344–15349.
- 3 J. Wang, W. Mao, L. L. Lock, J. Tang, M. Sui, W. Sun, H. Cui, D. Xu and Y. Shen, The Role of Micelle Size in Tumor Accumulation, Penetration, and Treatment, *ACS Nano*, 2015, **9**(7), 7195–7206.
- 4 H. R. Jia, Y. X. Zhu, X. Y. Liu, G. Y. Pan, G. Gao, W. Sun, X. D. Zhang, Y. W. Jiang and F. G. Wu, Construction of Dually Responsive Nanotransformers with Nanosphere-Nanofiber-Nanosphere Transition for Overcoming the Size Paradox of Anticancer Nanodrugs, *ACS Nano*, 2019, **13**(10), 11781–11792.
- 5 R. K. Jain and T. Stylianopoulos, Delivering nanomedicine to solid tumors, *Nat. Rev. Clin. Oncol.*, 2010, **7**(11), 653–664.
- 6 C. L. Waite and C. M. Roth, Nanoscale drug delivery systems for enhanced drug penetration into solid tumors: current progress and opportunities, *Crit. Rev. Biomed. Eng.*, 2012, **40**(1), 21–41.
- 7 S. D. Perrault, C. Walkey, T. Jennings, H. C. Fischer and W. C. Chan, Mediating tumor targeting efficiency of nanoparticles through design, *Nano Lett.*, 2009, **9**(5), 1909–1915.
- 8 P. Wardman, L. K. Folkes, S. M. Bentzen, M. R. Stratford, P. J. Hoskin, H. Phillips and S. Jackson, Influence of plasma glutathione levels on radiation mucositis, *Int. J. Radiat. Oncol., Biol., Phys.*, 2001, **51**(2), 460–464.
- 9 Y. Zhou, S. Hua, J. H. Yu, P. Dong, F. J. Liu and D. B. Hua, A strategy for effective radioprotection by chitosan-based long-circulating nanocarriers, *J. Mater. Chem. B*, 2015, **3**(15), 2931–2934.
- 10 X. Yang, M. Yang, B. Pang, M. Vara and Y. Xia, Gold Nanomaterials at Work in Biomedicine, *Chem. Rev.*, 2015, **115**(19), 10410–10488.
- 11 R. Brown, M. Tehei, S. Oktaria, A. Briggs, C. Stewart, K. Konstantinov, A. Rosenfeld, S. Corde and M. Lerch, High-Z Nanostructured Ceramics in Radiotherapy: First Evidence of Ta<sub>2</sub>O<sub>5</sub>-Induced Dose Enhancement on Radioresistant Cancer Cells in an MV Photon Field, *Part. Part. Syst. Charact.*, 2014, **31**(4), 500–505.
- 12 G. Song, C. Liang, X. Yi, Q. Zhao, L. Cheng, K. Yang and Z. Liu, Perfluorocarbon-Loaded Hollow Bi<sub>2</sub>Se<sub>3</sub> Nanoparticles for Timely Supply of Oxygen under Near-Infrared Light to Enhance the Radiotherapy of Cancer, *Adv. Mater.*, 2016, **28**(14), 2716–2723.
- 13 F. Klemm and J. A. Joyce, Microenvironmental regulation of therapeutic response in cancer, *Trends Cell Biol.*, 2015, **25**(4), 198–213.
- 14 M. Song, T. Liu, C. Shi, X. Zhang and X. Chen, Bioconjugated Manganese Dioxide Nanoparticles Enhance Chemotherapy Response by Priming Tumor-Associated Macrophages toward M1-like Phenotype and Attenuating Tumor Hypoxia, *ACS Nano*, 2016, **10**(1), 633–647.
- 15 Y. Liu, J. Sun, W. Cao, J. Yang, H. Lian, X. Li, Y. Sun, Y. Wang, S. Wang and Z. He, Dual targeting folate-conjugated hyaluronic acid polymeric micelles for paclitaxel delivery, *Int. J. Pharm.*, 2011, **421**(1), 160–169.
- 16 K. Y. Choi, H. Chung, K. H. Min, H. Y. Yoon, K. Kim, J. H. Park, I. C. Kwon and S. Y. Jeong, Self-assembled hyaluronic acid nanoparticles for active tumor targeting, *Biomaterials*, 2010, **31**(1), 106–114.
- 17 H. E. Barker, J. T. Paget, A. A. Khan and K. J. Harrington, The tumour microenvironment after radiotherapy: mechanisms of resistance and recurrence, *Nat. Rev. Cancer*, 2015, **15**(7), 409–425.
- 18 Y. Lou, P. C. McDonald, A. Oloumi, S. Chia, C. Ostlund, A. Ahmadi, A. Kyle, U. Auf dem Keller, S. Leung, D. Huntsman, B. Clarke, B. W. Sutherland, D. Waterhouse, M. Bally, C. Roskelley, C. M. Overall, A. Minchinton, F. Pacchiano, F. Carta, A. Scozzafava, N. Touisni, J. Y. Winum, C. T. Supuran and S. Dedhar, Targeting tumor hypoxia: suppression of breast tumor growth and metastasis by novel carbonic anhydrase IX inhibitors, *Cancer Res.*, 2011, **71**(9), 3364–3376.
- 19 S. E. Rademakers, P. N. Span, J. H. Kaanders, F. C. Sweep, A. J. van der Kogel and J. Bussink, Molecular aspects of tumour hypoxia, *Mol. Oncol.*, 2008, **2**(1), 41–53.



- 20 I. Lohse, C. Lourenco, E. Ibrahimov, M. Pintilie, M. S. Tsao and D. W. Hedley, Assessment of hypoxia in the stroma of patient-derived pancreatic tumor xenografts, *Cancers*, 2014, **6**(1), 459–471.
- 21 Y. Hao, L. Wang, B. Zhang, D. Li, D. Meng, J. Shi, H. Zhang, Z. Zhang and Y. Zhang, Manganese dioxide nanosheets-based redox/pH-responsive drug delivery system for cancer theranostic application, *Int. J. Nanomed.*, 2016, **11**, 1759–1778.
- 22 L. Meng, Y. Cheng, S. Gan, Z. Zhang, X. Tong, L. Xu, X. Jiang, Y. Zhu, J. Wu and A. Yuan, Facile Deposition of Manganese Dioxide to Albumin-Bound Paclitaxel Nanoparticles for Modulation of Hypoxic Tumor Microenvironment To Improve Chemoradiation Therapy, *Mol. Pharmaceutics*, 2018, **15**(2), 447–457.
- 23 Y. Feng, D. Ding, W. Sun, Y. Qiu, L. Luo, T. Shi, S. Meng, X. Chen and H. Chen, Magnetic Manganese Oxide Sweetgum-Ball Nanospheres with Large Mesopores Regulate Tumor Microenvironments for Enhanced Tumor Nanotheranostics, *ACS Appl. Mater. Interfaces*, 2019, **11**(14), 37461–37470.
- 24 J. Shi, R. Ma, L. Wang, J. Zhang, R. Liu, L. Li, Y. Liu, L. Hou, X. Yu, J. Gao and Z. Zhang, The application of hyaluronic acid-derivatized carbon nanotubes in hematoporphyrin monomethyl ether-based photodynamic therapy for in vivo and in vitro cancer treatment, *Int. J. Nanomed.*, 2013, **8**, 2361–2373.
- 25 T. H. Tran, J. Y. Choi, T. Ramasamy, D. H. Truong, C. N. Nguyen, H. G. Choi, C. S. Yong and J. O. Kim, Hyaluronic acid-coated solid lipid nanoparticles for targeted delivery of vorinostat to CD44 overexpressing cancer cells, *Carbohydr. Polym.*, 2014, **114**, 407–415.
- 26 C. R. Gordijo, A. Z. Abbasi, M. A. Amini, H. Y. Lip, A. Maeda, P. Cai, P. J. O'Brien, R. S. DaCosta, A. M. Rauth and X. Y. Wu, Design of Hybrid MnO<sub>2</sub>-Polymer-Lipid Nanoparticles with Tunable Oxygen Generation Rates and Tumor Accumulation for Cancer Treatment, *Adv. Funct. Mater.*, 2015, **25**(12), 1858–1872.
- 27 W. Fan, W. Bu, B. Shen, Q. He, Z. Cui, Y. Liu, X. Zheng, K. Zhao and J. Shi, Intelligent MnO<sub>2</sub> Nanosheets Anchored with Upconversion Nanoprobes for Concurrent pH-/H<sub>2</sub>O<sub>2</sub>-Responsive UCL Imaging and Oxygen-Elevated Synergetic Therapy, *Adv. Mater.*, 2015, **27**(28), 4155–4161.
- 28 H. Fan, Z. Zhao, G. Yan, X. Zhang, C. Yang, H. Meng, Z. Chen, H. Liu and W. Tan, A smart DNzyme-MnO<sub>2</sub> nanosystem for efficient gene silencing, *Angew. Chem., Int. Ed. Engl.*, 2015, **54**(16), 4801–4805.
- 29 C. He, D. Liu and W. Lin, Self-assembled core-shell nanoparticles for combined chemotherapy and photodynamic therapy of resistant head and neck cancers, *ACS Nano*, 2015, **9**(1), 991–1003.
- 30 K. F. Xu, H. R. Jia, Y. X. Zhu, X. Y. Liu, G. Gao, Y. H. Li and F. G. Wu, Cholesterol-Modified Dendrimers for Constructing a Tumor Microenvironment-Responsive Drug Delivery System, *ACS Biomater. Sci. Eng.*, 2019, **5**(11), 6072–6081.
- 31 T. D. Eubank, R. D. Roberts, M. Khan, J. M. Curry, G. J. Nuovo, P. Kuppasamy and C. B. Marsh, Granulocyte macrophage colony-stimulating factor inhibits breast cancer growth and metastasis by invoking an anti-angiogenic program in tumor-educated macrophages, *Cancer Res.*, 2009, **69**(5), 2133–2140.
- 32 C. C. Huang, W. T. Chia, M. F. Chung, K. J. Lin, C. W. Hsiao, C. Jin, W. H. Lim, C. C. Chen and H. W. Sung, An Implantable Depot That Can Generate Oxygen in Situ for Overcoming Hypoxia-Induced Resistance to Anticancer Drugs in Chemotherapy, *J. Am. Chem. Soc.*, 2016, **138**(16), 5222–5225.
- 33 H. M. Chen, J. H. He, C. B. Zhang and H. He, Self-assembly of novel mesoporous manganese oxide nanostructures and their application in oxidative decomposition of formaldehyde, *J. Phys. Chem. C*, 2007, **111**(49), 18033–18038.
- 34 M. A. Oberli, Lipid Nanoparticle Assisted mRNA Delivery for Potent Cancer Immunotherapy, *Nano Lett.*, 2017, **17**(3), 1326–1335.
- 35 P. Zhang, J. Wang, H. Chen, L. Zhao, B. Chen, C. Chu, H. Liu, Z. Qin, J. Liu, Y. Tan, X. Chen and G. Liu, Tumor Microenvironment-Responsive Ultrasmall Nanodrug Generators with Enhanced Tumor Delivery and Penetration, *J. Am. Chem. Soc.*, 2018, **140**(44), 14980–14989.

